PNAS RESEARCH ARTICLE | APPLIED PHYSICAL SCIENCES

Large complete and isotropic phononic band gaps in ultradense stealthy hyperuniform composites

Murray Skolnick[a] Paul J. Steinhardt[b,1] and Salvatore Torquato[a,b,c,d]

Affiliations are included on p. 9.

Contributed by Paul J. Steinhardt; received June 22 2026; accepted August 12 2026; reviewed by Tony Valier-Brasier Michele Diego and Houlong Zhuang

Complete phononic band gaps–frequency intervals that exclude elastic waves of every polarization–have so far been realized only in periodic phononic crystals whose band structures are direction-dependent and defect-sensitive. Disordered stealthy hyperuniform composites have produced complete and isotropic photonic band gaps but analogous elastic designs have so far fallen short. Here we show that pushing such composites to the ultradense inclusion packing fractions recently shown to be achievable–using stiff high-mass-density disk inclusions embedded in a compliant low-mass-density matrix–breaks this barrier. As inclusion packing fraction ϕ_2 increases the in-plane and out-of-plane polarization band gaps widen until they overlap yielding the first complete and isotropic phononic band gap which persists for systems as large as 4 000 disks. Full-wave finite-element calculations and Rayleigh quotient analysis show that conventional lower-packing-fraction stealthy hyperuniform composites never achieve this overlap because nearly contacting inclusion pairs and large matrix pore regions keep the two polarization gaps apart. Our analysis further reveals a general microstructural requirement for complete phononic–but not photonic–band gaps: a high-volume-fraction disconnected stiff phase embedded in a connected compliant matrix. These results establish a route to disordered media with large direction-independent phononic band gaps for shielding filtering and guiding elastic waves across length scales with potential applications ranging from thermal-phonon management in microdevices to sound vibration and seismic-wave insulation.

phononics | phononic band gaps | stealthy hyperuniformity | disordered materials | elastic waves

Significance

We present a technique for designing disordered two-phase media with complete phononic band gaps that block the transmission of elastic waves equally well in every direction and over a wide range of frequencies. A related feat has been achieved for electromagnetic waves using disordered stealthy hyperuniform networks of high-dielectric material, but applying the same strategy to elastic waves—stiff, high-mass-density disks embedded in a compliant, low-mass-density matrix—has so far failed to produce complete band gaps. The key advance enabling success here is a substantially closer packing of disks than had been previously achieved. These materials may enable robust, direction-independent elastic-wave shielding, filtering, and guiding across frequency ranges, from thermal-phonon manipulation to sound and seismic insulation.

Phononic solids are an emerging class of engineered multiphase materials whose microstructures are designed to control elastic waves, much as photonic solids control light, and can exhibit frequency intervals in which wave propagation is forbidden, i.e., phononic band gaps PBGs) [1–6]. Such materials are relevant to vibration and sound insulation, thermal management, ultrasound imaging, energy harvesting, and micro-/nano-electromechanical devices [6–12].

A central challenge for robust elastic wave control is to realize complete and isotropic PBGs that block elastic waves of all polarizations in all directions. Periodic phononic composites, including canonical architectures composed of stiff, high-mass-density nonoverlapping inclusions embedded in a compliant, low-mass-density matrix, can exhibit complete band gaps at sufficiently high inclusion volume fractions ϕ_2, but these gaps are direction-dependent because of the discrete symmetries of the underlying periodic microstructure and can be degraded or closed by structural perturbations [5, 13]. Disordered stealthy hyperuniform many-particle systems, whose structure factor $S(k)$ vanishes over a finite exclusion region about the origin in reciprocal space i.e., $S(k) = 0$ for $0 \quad k \quad K$) while being statistically isotropic and lacking Bragg peaks [14–17], have been shown in simulations and experiments to exhibit isotropic and complete photonic band gaps that are robust to defects [18–21].

These photonic results motivate analogous elastic designs, but electromagnetic and elastic waves obey different field equations and material interface conditions. Photonic gaps depend on dielectric contrast and electromagnetic boundary conditions [22], whereas phononic gaps depend on mass-density and elastic-modulus contrasts, coupled vector polarizations and mode conversion, and displacement- and traction-continuity conditions at bonded interfaces [5]. In two-dimensional 2D) photonics, the two polarizations favor different phase topologies, requiring connected high-dielectric networks decorated with cylindrical nodes so that both polarization gaps can open and overlap [18–22]. In phononics, by contrast, both polarizations favor disconnected stiff, high-mass-density inclusions embedded in a connected compliant, low-mass-density

Author contributions: M.S., P.J.S., and S.T. designed research; performed research; analyzed data; and wrote the paper.

Reviewers: T.V.-B., Institut Jean Le Rond d'Alembert, Sorbonne Université, CNRS; M.D., Institute of Industrial Science The University of Tokyo; and H.Z., Arizona State University.

Competing interest statement: Title: Ultradense stealthy hyperuniform materials with complete isotropic phononic bandgaps Application No. 63/947,332.

Copyright 2026 the Author s). Published by PNAS. This article is distributed under Creative Commons Attribution-NonCommercial-NoDerivatives License 4.0 CC BY-NC-ND).

[1]To whom correspondence may be addressed. Email: steinh@princeton.edu.

This article contains supporting information online at https://www.pnas.org/lookup/suppl/doi:10.1073/pnas.2622259123/-/DCSupplemental.

Published September 18, 2026.

Downloaded from https://www.pnas.org by PRINCETON UNIV LIBRARY; ACQUISITION SERVICE PERIODICALS on September 18, 2026 from IP address 140.180.240.88.

matrix 5), which we show in Section 3 follows from the bonded elastic interface conditions. The only prior stealthy phononic study found an isotropic but incomplete gap in a small, single arrangement of stiff, nonoverlapping inclusions 23), leaving open which additional microstructural features are needed for complete PBGs that persist at large system sizes. Apart from this single study, complete band gap formation in disordered stealthy hyperuniform phononic media has not been systematically investigated.

To advance the state of the art, we propose to combine the statistical isotropy and intermediate- to long-wavelength uniformity of stealthy disorder with the high packing fraction, locally uniform inclusion environments known to yield complete band gaps in phononic crystals 5). We accomplish this task by exploiting a recently introduced class of "ultradense" high packing fraction) stealthy hyperuniform disk configurations 30, 31) as templates for disordered two-phase elastic composites consisting of stiff, high-mass-density disk inclusions embedded in a compliant, low-mass-density matrix, or equivalently, a 3D transversely isotropic phononic solid composed of aligned cylinders in place of the disks. We show that these ultradense designs exhibit the first complete and isotropic phononic band gaps and systematically explore their gap width dependence on the stealthiness parameter χ and inclusion volume fraction ϕ_2 via comprehensive full-wave finite-element calculations.

Because the standard collective-coordinate optimization procedure to generate stealthy hyperuniform ground states does not enable one to achieve high packing fractions 32, 33), Kim and Torquato 30, 31) devised a modified scheme that uses a short-range soft-core repulsive potential in addition to the "stealthy" long-range potential. This modification accurately produces stealthy hyperuniform ground states that enable one to create packings with appreciably higher maximum packing fractions $\phi_2^{\max)}$. We identify regimes in which the out-of-plane and in-plane polarization gaps overlap to form complete gaps whose widths can be tuned by varying the stealthiness parameter χ and ϕ_2, and we show that these complete, isotropic gaps persist for systems as large as $N = 4{,}000$ disks. To the best of our knowledge, this work represents the first study of the phononic properties of ultradense stealthy hyperuniform two-phase composites, specifically determining their phononic band-gap characteristics using full-wave simulations; the only previous investigation of the physical properties of such systems was a very recent study that did not consider phononic behavior 34). To isolate the role of ultradensity, we also compare these systems with conventional stealthy hyperuniform phononic composites at comparable χ and ϕ_2. The conventional stealthy composites fail to open complete gaps, showing that high inclusion packing fraction alone is insufficient. Through analysis of the gap-edge modes, we find that nearly contacting inclusion pairs host modes that push the lower band edge upward, while large matrix pores host modes that pull the upper band edge downward, thereby narrowing the interval over which the polarization-resolved gaps can overlap. Complete PBG formation therefore requires the distinctive combination realized by ultradense stealthy hyperuniform media: stealthy long-wavelength order, high inclusion packing fraction, and suppressed nearest-neighbor and pore-size fluctuations.

We distinguish phononic band gaps in elastic solids from acoustic band gaps in scalar pressure-wave systems, such as solid scatterers embedded in a fluid, rather than in a compliant, low-mass-density solid as considered here. Such scalar acoustic systems do not involve the coupled vector polarizations, mode conversion, or bonded-interface conditions that control complete elastic band gaps, although stealthy acoustic media can exhibit band gaps and transparency 24–29).

1. Model Systems and Band Gap Diagnostics

1.1. Ultradense Stealthy Hyperuniform Two-Phase Media. We study disordered 2D transversely isotropic phononic composites formed by embedding disk inclusions in a connected matrix. The inclusion centers are obtained from ultradense stealthy hyperuniform point configurations in the isotropic regime 0 χ 1/2 14, 35). For a single configuration, stealthiness means that the structure factor vanishes over a finite exclusion region around the origin, i.e., $S(\mathbf{k}) = 0$ for 0 $|\mathbf{k}|$ K, and the degree of stealthiness is quantified in two dimensions by $\chi = K^2/(16\pi\rho)$, where ρ is the number density 16).

Ultradense configurations supplement the usual stealthy constraints with a short-range soft-core repulsion, as described in *Materials and Methods*. This additional local constraint leads to finite, system-size-insensitive maximal inclusion volume fractions $\phi_2^{\max)}(\chi)$ and suppresses nearest-neighbor fluctuations relative to conventional stealthy configurations 30, 31). Here, we consider for each $\chi \in (0, 1/2)$ an ensemble of ultradense configurations generated at $\phi_2^{\max)}(\chi)$. We convert these point configurations into two-phase elastic composites by decorating the points with identical, nonoverlapping disks of radius R, so that the inclusion volume fraction is $\phi_2 = \rho\pi R^2 \le \phi_2^{\max)}$. This construction separates the effects of stealthy long-wavelength order, controlled by χ, from those of inclusion packing fraction and local geometry, controlled by ϕ_2 and the ultradense soft-core constraint.

In all simulations, phase 2 is the stiff, high-mass-density inclusion phase, and phase 1 is the compliant, low-mass-density matrix phase. Specifically, we use steel disks embedded in an epoxy matrix as a representative high-contrast linearly elastic composite 4, 5); the material parameters are given in *Materials and Methods*. We set the number density to unity, so that the characteristic interparticle spacing is $a = \rho^{1/2} = 1$, which we take to be in units of micrometers in our simulations. Thus, the resulting band gaps for the steel/epoxy composites considered here lie in the ultrasonic-to-hypersonic frequency range; other frequency regimes can be reached by changing the physical value assigned to a and/or by varying the material parameters. Representative ultradense and conventional stealthy configurations and their structure factors are shown in Fig. 1.

1.2. Polarization-Resolved and Complete Phononic Band Gaps. For the band gap calculations, we treat each finite configuration as a supercell of area under periodic boundary conditions. For each chosen Bloch wavevector $\mathbf{k}$, the elastic modes satisfy Bloch boundary conditions on the supercell, and we denote the resulting eigenfrequencies of the entire supercell by ω_i. Because the composites are transversely isotropic, the elastic eigenmodes separate into out-of-plane and in-plane polarized modes. We identify band gaps separately for the out-of-plane and in-plane polarization spectra. Here and throughout, "isotropic" means that, within numerical resolution, the gap edges, and hence the gap width, do not vary with the direction of the Bloch wavevector $\mathbf{k}$. We define the complete phononic band gap to be the frequency interval over which both polarizations are forbidden for all directions. Given the isotropy of the phononic band gaps of the ultradense systems see Section 2 for details), all band gaps reported in the main text were evaluated at the supercell $= (0, 0, 0)$ Bloch wavevector, which we note is computationally less expensive than sampling nonnull wavevectors 5).

Downloaded from https://www.pnas.org by PRINCETON UNIV LIBRARY; ACQUISITION SERVICE PERIODICALS on September 18, 2026 from IP address 140.180.240.88.

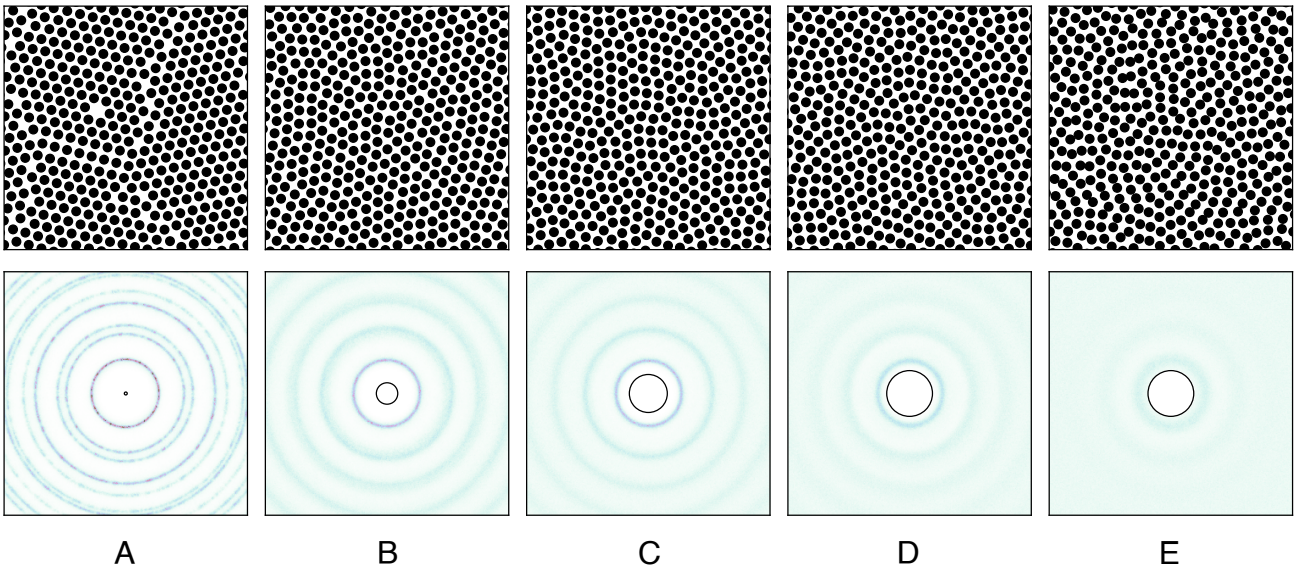


Fig. 1. Images of *Top* row) stealthy hyperuniform disk packings at inclusion volume fraction $\phi_2 = 0.40$ and *Bottom* row) their corresponding structure factors, S **k**), across χ and $\phi_2^{\max)}$ values: ultradense) $\chi = 0.002$ and $\phi_2^{\max)} = 0.86$, *B*) $\chi = 0.10$ and $\phi_2^{\max)} = 0.82$, *C*) $\chi = 0.30$ and $\phi_2^{\max)} = 0.77$, *D*) $\chi = 0.45$ and $\phi_2^{\max)} = 0.68$, and conventional *E*) $\chi = 0.45$ and $\phi_2^{\max)} = 0.40$. In the structure factors in the *Bottom* row, white blue) hues correspond to low high) scattering intensity, and the superimposed black circles with radius K encompass the stealthy exclusion region. As χ increases toward 1/2, the rings in S **k**) become more diffuse and lower in intensity, reflecting the transition from polycrystalline structures to structures with greater local disorder. Due to the absence of a soft-core repulsion, the $\chi = 0.45$ conventional stealthy system in *E*) has many nearly contacting inclusions and broader local geometric fluctuations than the corresponding ultradense packing in *D*).

For each polarization-resolved or complete gap, we report the gap-midgap ratio 5, 18, 22, 23)

$$\frac{\Delta\omega}{\omega_m} = \frac{2(\omega_+ \quad \omega \quad)}{\omega_+ + \omega}, \qquad [\ ]$$

where $\Delta\omega = \omega_+ \quad \omega$ is the gap width, $\omega_m = (\omega_+ + \omega \quad)/2$ is the midgap frequency, and ω and ω_+ are the lower and upper gap-edge frequencies, respectively. To assess whether apparent complete gaps in finite samples persist at larger system sizes, we compute for each polarization the area-normalized phononic density of states 21)

$$(\omega) = -\frac{1}{} \sum_{i=1}^{\infty} \delta(\omega \quad \omega_i), \qquad [2]$$

which is evaluated at the -point. For each parameter set and system size, we pool the eigenfrequencies from an ensemble of independent configurations to construct the ensemble-averaged density of states.

Following Klatt et al. 21), we distinguish between two asymptotic band tail behaviors of (ω). For an exponential tail, the density of states has no strict band edge and is described by $(\omega) \sim \exp(\pm\beta_\pm\omega)$, where $\beta_\pm > 0$, implying that the upper and lower tails must eventually cross and close the apparent gap at a finite minimum density of states, $_{\min}$. By contrast, a power-law tail is defined with respect to a well-defined edge frequency $\omega_\pm$ and has the form $(\omega) \sim |\delta\omega_\pm|^{\gamma_\pm}$, where $\delta\omega_\pm = \omega \quad \omega_\pm$, so that the density of states vanishes as $\omega \to \omega_\pm$. If the lower and upper power-law tails for a given polarization are sufficiently separated in frequency, a finite interval can remain in which $(\omega) = 0$, consistent with a true phononic band gap rather than a deep pseudogap 21). The numerical procedures used to compute the spectra, finite-system density of states histograms, band-tail fits, and gap statistics are described in *Materials and Methods*.

2. Results

2.1. Complete and Isotropic PBGs Across the Ultradense Design Space. We first quantify phononic band-gap formation across the ultradense χ–ϕ_2 design space by computing the gap-midgap ratio $\Delta\omega/\omega_m$ for the out-of-plane, in-plane, and complete gaps. As shown in Fig. 2, the out-of-plane polarization gaps are large over much of the accessible parameter space, whereas the in-plane polarization gaps are narrower and therefore generally limit the complete gap, which corresponds to the intersection of the two gaps. Ensemble-averaged values and SDs of the polarization-resolved and complete gap–midgap ratios $\Delta\omega/\omega_m$ are listed in *SI ppendix*, Tables S1–S3. Complete PBGs arise only where the out-of-plane and in-plane forbidden intervals overlap in frequency, which restricts the region of full polarization-independent wave blocking.

The heatmaps reveal a pronounced nonmonotonic dependence of the complete gap width on both χ and ϕ_2. At low inclusion packing fractions, the complete gap is absent or small even when the underlying point pattern is stealthy. For fixed χ, increasing ϕ_2 initially widens the polarization-resolved gaps and promotes their overlap, but the complete gap reaches a maximum at intermediate-to-large ϕ_2 i.e., 0.5 ϕ_2 0.6) before decreasing again near the largest accessible packing fractions. Likewise, for fixed ϕ_2, the complete gap generally increases from the smallest χ values to comparable values at $\chi = 0.30$ and $\chi = 0.40$, before decreasing at $\chi = 0.45$ *SI ppendix*, Fig. S1). Thus, neither maximal packing fraction nor maximal stealthiness alone optimizes complete PBG formation.

The largest complete gaps occur for intermediate stealthiness and moderately high packing fraction. Among the systems considered here, the widest complete gap is obtained for $\chi = 0.30$ and $\phi_2 = 0.60$, with ensemble-averaged gap-midgap ratios of $\Delta\omega/\omega_m = 93.81 \pm 1.14$ for out-of-plane modes, 70.7 ± 1.6 for in-plane modes, and 45.5 ± 1.5 for the

Downloaded from https://www.pnas.org by PRINCETON UNIV LIBRARY; ACQUISITION SERVICE PERIODICALS on September 18, 2026 from IP address 140.180.240.88.

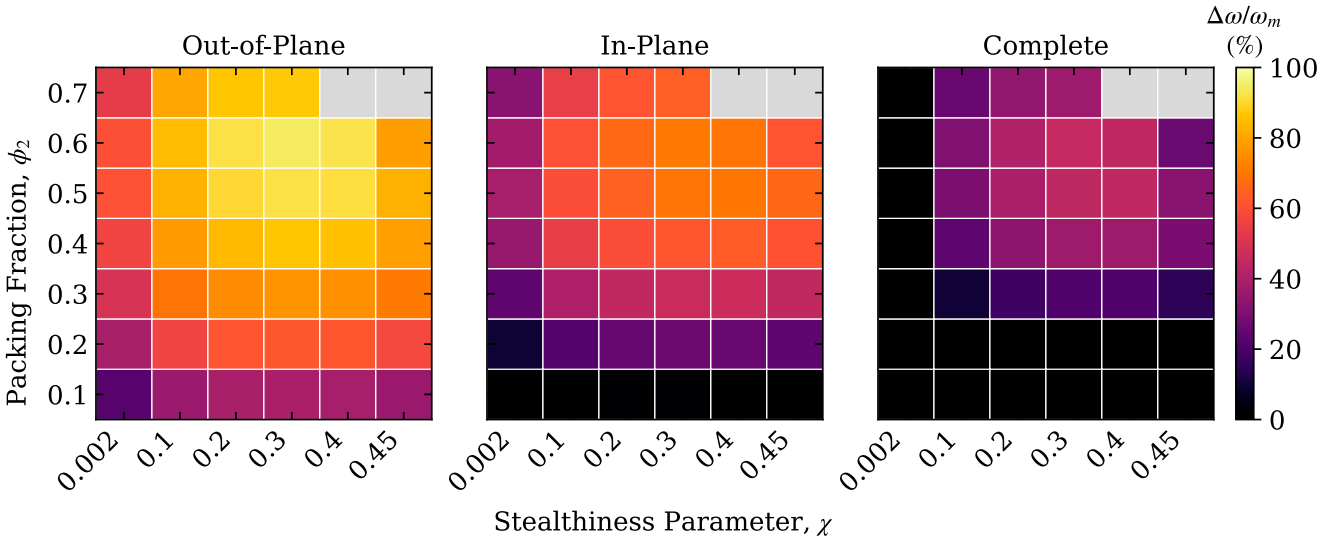


Fig. 2. Gap-midgap ratio $\Delta\omega/\omega_m$ for out-of-plane, in-plane, and complete phononic band gaps at the -point in $N = 400$ disk ultradense composites across values of the stealthiness parameter χ and inclusion packing fraction ϕ_2. Values are ensemble averages over independent realizations. Black cells denote parameter values for which no corresponding gap is present, while gray cells denote packing fractions that are inaccessible because they exceed $\phi_2^{\max)}$ χ). The out-of-plane gaps are broad over much of the accessible parameter space, whereas the in-plane gaps are narrower and therefore limit the complete gap. All gaps exhibit a nonmonotonic dependence on both χ and ϕ_2, with the largest gaps occurring at intermediate stealthiness and moderately high packing fraction.

complete gap. Here, the uncertainties are ensemble SDs over independent configurations. Note that the complete gap width of the $\chi = 0.30$, $\phi_2 = 0.60$ ultradense system approaches those of certain steel-epoxy phononic crystals at the same ϕ_2: We found computationally that disks arranged on the square and triangular lattices respectively have complete gap-midgap ratios 58.2 and 82.4 .

We expect that the band gaps of the ultradense phononic composites are isotropic given that they are statistically isotropic and conventional stealthy structures are well known to exhibit isotropic band gaps 18–20, 23). We verify this isotropy by computing the density of states for a representative ensemble of $N = 400$ disk $\chi = 0.30$ and $\phi_2 = 0.60$ configurations at Bloch wavevectors X $= (\pi/L, 0, 0)$ and M $= (\pi/L, \pi/L, 0)$, where L is the supercell side length. As seen in *SI ppendix*, Fig. S2 and Table S4, the ensemble-averaged density of states and band-edge frequencies are virtually identical at the -, X- and M-points. These trends show that wide, isotropic and complete phononic gap formation in ultradense composites is controlled by a competition between increasing reciprocal-space order, which favors the opening of robust gaps, and real-space packing constraints, which determine whether the polarization-resolved gaps open and overlap, as we will show below.

2.2. Persistence of Complete PBGs to Large System Sizes. To assess whether the apparent complete phononic gaps identified for finite-size ultradense samples remain open as the system size increases, we examine the scaling of the density of states near the lower and upper gap edges for large ensembles of $N = 4{,}000$ disk composites at fixed $\phi_2 = 0.40$. We did not extend the large-N band-tail analysis to the $\chi = 0.30$, $\phi_2 = 0.60$ design, which has the widest gap among the systems considered here, because mesh generation and eigenvalue calculations become appreciably more demanding as the packing fraction increases.

As seen in Fig. 3 , the $N = 4{,}000$ disk $\chi = 0.002$ system exhibits only nonoverlapping pseudogaps for the two polarizations, each with 10^8 $_{\min}$ 10^9 and apparently exponential upper tails. Given the highly polycrystalline structure of the $\chi = 0.002$ composites, we hypothesize that the various structural defects e.g., vacancies and grain boundaries; see Fig. 1) are associated with the gaps closing. This behavior contrasts with that of the corresponding $N = 400$ systems, which appeared to show disjoint gaps for the individual polarizations, underscoring the importance of large-system ensemble-based analyses for distinguishing true complete phononic band gaps from finite-size pseudogaps in disordered systems.

By contrast, the $\chi = 0.30$ and $\chi = 0.45$ composites exhibit tail behavior that is consistent with power-law scaling for both polarizations, as seen in Fig. 3 *B* and *C*. The $N = 4{,}000$ gap-midgap ratios are close to their $N = 400$ counterparts. For $\chi = 0.30$, the $N = 4{,}000$ out-of-plane, in-plane, and complete gaps are respectively 83.85 ± 0.75 , 60.82 ± 0.50 , and 35.35 ± 0.82 , compared to the corresponding $N = 400$ values of 86.0 ± 0.9 , 62.1 ± 0.7 , and 37.2 ± 1.1 . For $\chi = 0.45$, the $N = 4{,}000$ values are 76.94 ± 0.38 , 59.75 ± 0.40 , and 28.02 ± 0.39 , compared to the corresponding $N = 400$ values of 78.5 ± 0.9 , 60.9 ± 0.5 , and 29.6 ± 0.9 . This behavior suggests that the corresponding complete phononic band gaps might remain open at even larger system sizes. Whether the gap remains open for arbitrarily large sizes cannot be determined from simulations, and remains an open theoretical issue.

Analysis of the $\chi = 0.10$, $N = 4{,}000$ disk ensemble shows an apparent complete phononic band gap whose lower band tails are compatible with power-law scaling, while the upper tails are too noisy to classify unambiguously; see *SI ppendix*, Fig. S3. We therefore interpret $\chi = 0.10$ as being near the critical χ value associated with the crossover between pseudogaps and band gaps in ultradense phononic composites. Altogether, these results suggest that, as with the case of stealthy photonics 21), sufficiently strong stealthiness—and thus a high degree of order across short-, intermediate-, and large-length scales—is required not only to open a complete phononic gap in finite ultradense samples, but also to prevent that gap from closing and becoming a pseudogap as the system size increases.

Downloaded from https://www.pnas.org by PRINCETON UNIV LIBRARY; ACQUISITION SERVICE PERIODICALS on September 18, 2026 from IP address 140.180.240.88.

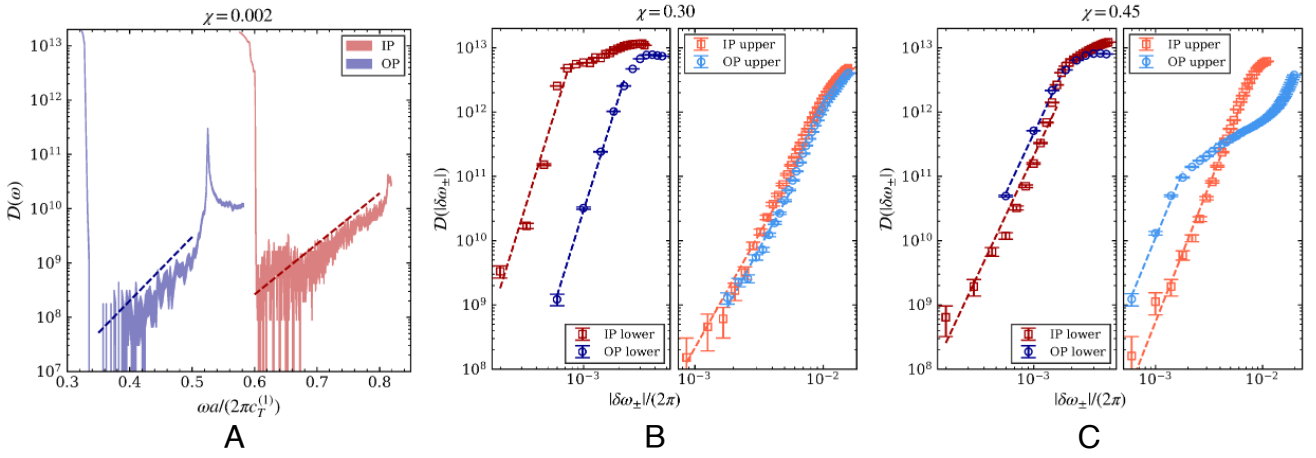


Fig. 3.) Log-scale plots of the out-of-plane OP) and in-plane IP) density of states ω) for $\chi = 0.002$ ultradense phononic solids. Log–log plots of the density of states tails near the gap edges $|\delta\omega_{\pm}|$) for *B*) $\chi = 0.30$ and *C*) $\chi = 0.45$. The dashed lines represent the exponential upper tails of the pseudogaps in), and the power-law scaling of the lower- and upper-band tails in *B* and *C*). SEs are represented by the shaded regions in), and error bars in *B* and *C*). All results are for ensembles of systems with $N = 4{,}000$ disk inclusions.

3. Explanation of PBG Formation

The results above raise three related questions: Why do disconnected stiff inclusions in a connected compliant matrix lead to phononic band gaps? Why does increasing the inclusion volume fraction ϕ_2 widen the in-plane and out-of-plane gaps? How does ultradensity cause the gaps to overlap? We address these questions using the elastic Rayleigh quotient, the bonded elastic interface conditions, and qualitative differences between the inclusion nearest-neighbor and matrix pore-size distributions of ultradense and conventional stealthy composites.

3.1. Phase Topology. For a given Bloch-periodic elastic eigenmode with displacement field $\mathbf{u}(\mathbf{x})$ in a periodic supercell Ω that comprises the entire two-phase medium, the variational principle for linear elastodynamics gives ω^2 as the stationary value of the elastic Rayleigh quotient 5):

$$\omega^2 = \frac{U}{K} = \frac{\int_{\Omega} (\mathbf{x}) : \mathbf{C}(\mathbf{x}) : (\mathbf{x})\, d\mathbf{x}}{\int_{\Omega} \rho_m(\mathbf{x})|\mathbf{u}(\mathbf{x})|^2\, d\mathbf{x}}. \qquad [3]$$

Here, U and K are respectively the strain- and kinetic-energy of the mode, the local strain is $(\mathbf{x}) = (\nabla\mathbf{u} + \nabla\mathbf{u}^T)/2$, and $\mathbf{C}(\mathbf{x})$ and $\rho_m(\mathbf{x})$ are respectively the local stiffness tensor and mass density. We take phase 2 to be the stiff, high-mass-density inclusion phase and phase 1 to be the compliant, low-mass-density matrix phase, with mass densities $\rho_m^{2)} > \rho_m^{1)}$ and Lamé parameters $\mu^{2)} > \mu^{1)}$ and $\lambda^{2)} > \lambda^{1)}$.

Across a bonded elastic interface, the displacement and traction satisfy

$$[\mathbf{u}] = 0, \qquad [\boldsymbol{\sigma}\hat{\mathbf{n}}] = 0, \qquad [4]$$

where $\boldsymbol{\sigma} = \mathbf{C} :$ and $\hat{\mathbf{n}}$ is the interface unit normal. For an out-of-plane mode $\mathbf{u} = w(x,y)\hat{\mathbf{z}}$, the relevant strains are shear strains proportional to gradients of w. Near an interface, the tangential and normal components are respectively written as $\partial_t w$ and $\partial_n w$, so that the corresponding strain-energy contributions in phase i scale as $U_t^{i)} \sim \mu^{i)}(\partial_t w^{i)})^2$ and $U_n^{i)} \sim \mu^{i)}(\partial_n w^{i)})^2$. Displacement continuity fixes $\partial_t w$ across the interface, while traction continuity fixes $\mu\partial_n w$. Thus,

$$\frac{U_t^{2)}}{U_t^{1)}} = \frac{\mu^{2)}}{\mu^{1)}}, \qquad \frac{U_n^{2)}}{U_n^{1)}} = \frac{\mu^{1)}}{\mu^{2)}}, \qquad [5]$$

with analogous in-plane estimates given in *SI ppendix*. Thus, the same tangential interfacial deformation is more energetically costly in the stiff phase than in the compliant matrix phase.

This interface constraint explains why low-Rayleigh-quotient modes favor disconnected stiff inclusions in a connected compliant matrix. The inclusions can undergo nearly rigid translation and rotation, contributing strongly to the kinetic-energy denominator K because of their high mass density, while the connected compliant matrix stores most of the strain energy. Increasing the inclusion-to-matrix mass-density contrast further reduces the lower band edge frequency through K. The nearly rigid disk motions below the gap suggest a local-resonance contribution, consistent with previous studies linking the frequencies of cylinder resonances and phononic band edges 23). A connected stiff matrix would inevitably lead to tangential deformation of the stiff phase and thus an increase in the strain-energy numerator U.

We verify this phase-energy partitioning using the phase 2 kinetic- and strain-energy concentration factors $K^{2)}$ and $U^{2)}$, which are defined in *Materials and Methods*. Fig. 4 shows that modes below the gaps have large inclusion kinetic-energy concentration, whereas modes above the gaps shift kinetic-energy weight into the matrix. By contrast, $U^{2)}$ remains small for both polarizations and packing fractions, confirming that the strain energy is concentrated primarily in the compliant matrix. This spatial distribution of energy for an in-plane mode right below the gap is shown directly in Fig. 4*B*.

3.2. High Inclusion Packing Fractions. Increasing ϕ_2 widens the polarization-resolved gaps by separating their lower and upper band edges. For lower-edge modes, increasing the volume of phase 2 increases the high-mass-density inclusion contribution to the kinetic-energy denominator,

$$K = \int_{\Omega_1} \rho_m^{1)}|\mathbf{u}(\mathbf{x})|^2\, d\mathbf{x} + \int_{\Omega_2} \rho_m^{2)}|\mathbf{u}(\mathbf{x})|^2\, d\mathbf{x}, \qquad [6]$$

Downloaded from https://www.pnas.org by PRINCETON UNIV LIBRARY; ACQUISITION SERVICE PERIODICALS on September 18, 2026 from IP address 140.180.240.88.

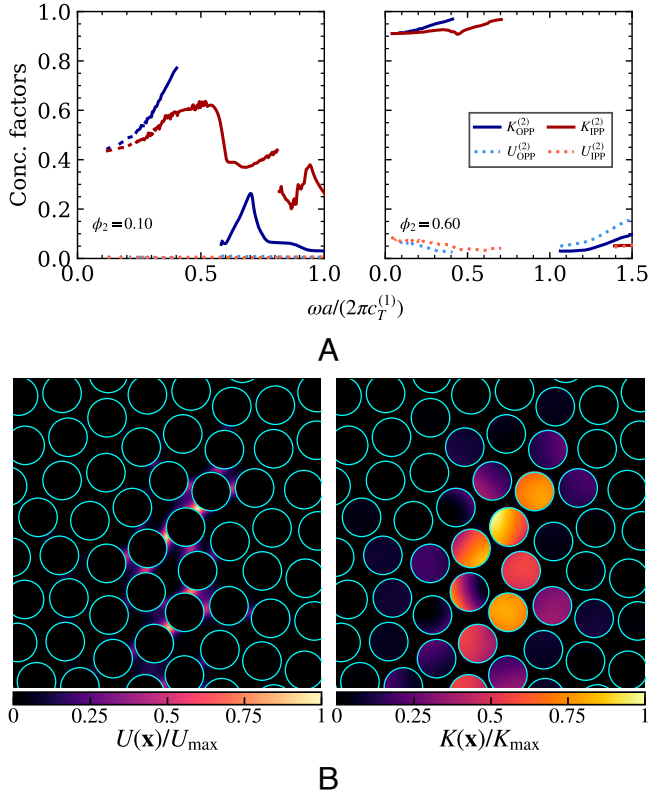


Fig. 4.) Phase 2 kinetic- and strain-energy concentration factors for the $\chi = 0.30$ ultradense system at $\phi_2 = 0.10$ and $\phi_2 = 0.60$. *B*) Normalized local strain- and kinetic-energy densities for the highest-frequency in-plane mode below the gap at $\chi = 0.30$ and $\phi_2 = 0.60$. The inclusion boundaries in *B*) are highlighted in cyan.

where Ω_1 and Ω_2 are the disjoint volumes occupied by the matrix and inclusion phases, respectively. Because $\rho_m^{2)} > \rho_m^{1)}$, nearly rigid inclusion-dominated modes can increase K without a comparable increase in U, lowering the lower band edge.

Modes above the gap are constrained by orthogonality and cannot reproduce these coherent inclusion motions. They instead shift kinetic-energy weight into the connected matrix and incur a confinement penalty in the narrow matrix channels. A mode confined to a channel of characteristic width h varies over a length scale of order h, giving $|\nabla \mathbf{u}| \sim |\mathbf{u}|/h$ and hence the frequency of such confined channel modes scales as $\omega_{\mathrm{ch}} \sim c_1/h$, where c_1 is the matrix wave speed; see *SI Appendix*. Thus, increasing ϕ_2 lowers the lower band edge through rigid translations and rotations of the disks and raises the upper band edge through narrow matrix channels, as seen in Fig. 5.

3.3. Ultradensity and Complete PBG Formation. We finally address why ultradensity is needed for the polarization-resolved gaps to overlap. At $\chi = 0.45$ and $\phi_2 = 0.30$, Fig. 5 shows that the conventional stealthy system has narrower in-plane and out-of-plane polarization gaps that do not overlap, whereas the ultradense system opens a complete gap. The representative modes in Fig. 6 indicate that this gap narrowing is associated with nearly contacting inclusion pairs and large matrix pore-like regions in conventional stealthy hyperuniform composites.

Specifically, the lower band edge is pushed upward by nearly contacting inclusion pairs. For inclusions of radius R, the surface-to-surface neck width between neighboring inclusions is

$$h_{ij} = r_{ij} \quad 2R. \qquad [7]$$

Thus, an excess of close-neighbor pairs in the nearest-neighbor distribution $H_P(r)$ directly produces an excess of narrow interinclusion matrix necks. As detailed quantitatively in ref. 31, conventional stealthy structures contain appreciably more inclusion close-neighbor pairs than ultradense systems at comparable χ. These dimer-like defects constrain the relative motion of neighboring, nearly rigid inclusions: as the intervening matrix neck narrows, its effective spring stiffness increases, thereby shifting the localized lower-edge modes upward in frequency. Fig. 6 shows such a dimer-localized lower-edge mode in the conventional system, which is absent in the ultradense system.

The upper band edge is pulled downward by large matrix pores and wide channels. These regions are quantified by the pore-size density $P(\delta)$, which is the probability density for the distance δ from a randomly chosen point in the matrix phase to the nearest inclusion surface 36). Because larger pores correspond to larger effective channel widths h, they host lower-frequency matrix-confined modes. Fig. 6*B* shows directly that the conventional stealthy upper-edge mode occupies a larger pore-like region than the corresponding ultradense mode, illustrating how such regions shift the upper edge frequency downward. Forthcoming analyses show that ultradense systems have narrower pore-size distributions than conventional stealthy systems at comparable χ and ϕ_2 37).

In conventional stealthy composites, these two types of localized modes shift the relevant band edges toward each other. By contrast, ultradense two-phase composites suppress both nearly contacting inclusion pairs and large matrix pores, preserving sufficiently wide polarization-resolved gaps for them to overlap into a complete PBG.

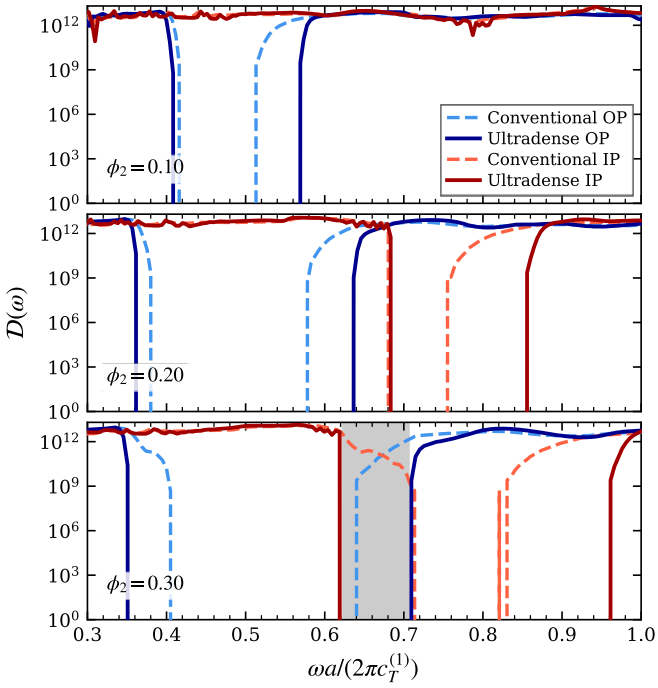


Fig. 5. Density of states for conventional and ultradense phononic composites at fixed $\chi = 0.45$ and increasing ϕ_2. Increasing ϕ_2 separates the lower and upper band edges, while ultradensity further widens the gaps, especially for in-plane modes. At $\phi_2 = 0.30$, only the ultradense system opens a complete gap, which is highlighted by the transparent gray region.

Downloaded from https://www.pnas.org by PRINCETON UNIV LIBRARY; ACQUISITION SERVICE PERIODICALS on September 18, 2026 from IP address 140.180.240.88.

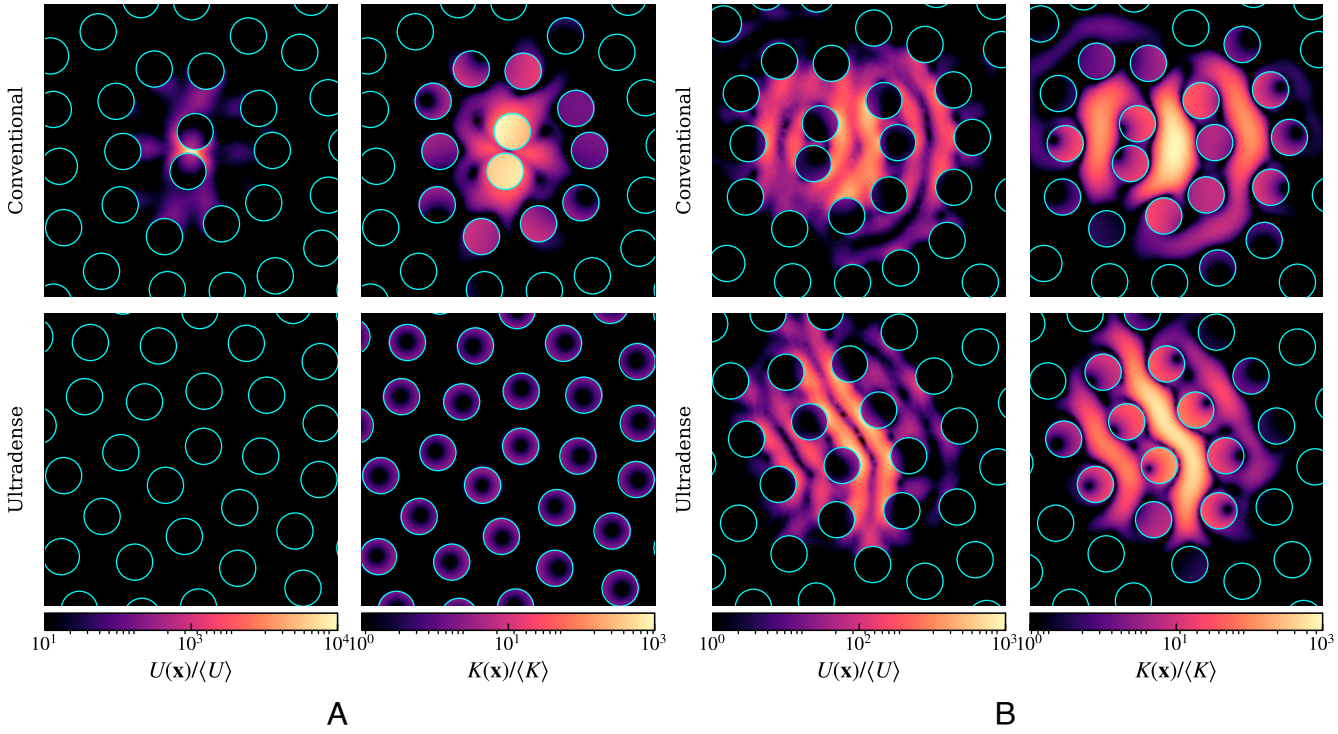


Fig. 6.) Normalized local strain-energy density U **x**)$/\langle U\rangle$ and kinetic-energy density K **x**)$/\langle K\rangle$ for representative highest frequency lower-edge in-plane polarization modes in conventional and ultradense systems at $\chi = 0.45$ and $\phi_2 = 0.30$, where $\langle X\rangle = |\Omega|^{-1}\int_\Omega X$ **x**) d**x**. *B*) Corresponding normalized energy densities for representative lowest frequency upper-edge modes.

4. Concluding Remarks

We have shown that ultradense stealthy hyperuniform two-phase composites provide a route to complete and isotropic phononic band gaps in disordered 2D transversely isotropic materials. This behavior contrasts with that of periodic phononic crystals, whose complete gaps are generally anisotropic, and previously studied nonultradense stealthy hyperuniform composites, which exhibit isotropic but incomplete gaps. Our results show that complete gap formation is controlled by a competition between reciprocal-space stealthy order and real-space packing constraints. Increasing χ strengthens stealthy correlations, but in ultradense two-phase composites it also reduces the maximal attainable inclusion volume fraction. As a consequence, the complete gap width is nonmonotonic in χ and is optimized at intermediate stealthiness, where the system retains sufficiently strong stealthy order while still allowing high inclusion packing fractions.

The elastic Rayleigh quotient analysis explains physically why disconnected stiff, high-mass-density inclusions embedded in a connected compliant, low-mass-density matrix are a successful topology. Bonded interface conditions make tangential deformation energetically costly in the stiff phase, so low-frequency modes lower the quotient by moving the high-mass-density disks nearly rigidly while storing most strain in the compliant matrix. This analysis also explains why photonic network architectures cannot be employed for phononic applications: Because the stiff walls are connected, their motion necessarily involves stiff-phase deformation, so the kinetic-energy benefit of their high mass density is offset by substantial strain-energy participation. In the stiff inclusion topology, increasing ϕ_2 lowers the lower band edge through rigid motion of the disks, while raising the upper band edge by concentrating strain in the narrow matrix channels between disks.

Ultradensity is essential because it suppresses the two local geometric defects that would otherwise close the complete gap: nearly contacting inclusion pairs, which push the lower band edge upward, and large matrix pores, which pull the upper band edge downward. As a control, we also tested a phase-inverted Delaunay-centroidal photonic-network architecture 18) in which the cellular domains form the stiff, high-mass-density inclusion phase and the connected network walls form the compliant, low-mass-density matrix; this nominally favorable topology exhibits only phononic pseudogaps rather than a complete PBG over the tested volume fractions *SI ppendix*, Figs. S4 and S5). Together, these results show that complete PBG formation in ultradense disk composites requires stealthy hyperuniform order, high inclusion packing fraction, and suppression of nearly contacting inclusion pairs and large matrix pore-like regions.

The band-tail analysis further shows that pronounced forbidden intervals in finite samples do not necessarily imply a true gap at larger system sizes. The smallest-χ case is consistent with deep pseudogaps, whereas the moderate- and large-χ cases are consistent with complete gaps that remain open to the extent resolvable in the present large-N calculations. Thus, sufficiently high stealthiness appears to be required not only to open a complete phononic gap, but also to stabilize it against finite-size closure. More broadly, the comparison with photonic stealthy hyperuniform media shows that stealthy long-wavelength order is a transferable organizing principle for isotropic wave gaps, but that the optimal local phase topology is determined by the specific field equations and interface conditions of the wave problem. Ultradense composites therefore provide a controlled setting in which reciprocal-space order and real-space packing can be tuned separately, making them useful both for designing isotropic phononic band-gap materials and for understanding

Downloaded from https://www.pnas.org by PRINCETON UNIV LIBRARY; ACQUISITION SERVICE PERIODICALS on September 18, 2026 from IP address 140.180.240.88.

how correlated disorder shapes elastic-wave propagation in heterogeneous media.

Several future directions remain open. First, the present analysis could be extended to fully three-dimensional 3D) ultradense stealthy hyperuniform two-phase composites, where the same interplay between stealthy disorder and local inclusion packing constraints may provide a route to complete and isotropic PBGs in 3D. Second, a Helmholtz decomposition of the in-plane eigenmodes 23) could be used to construct longitudinal- and transverse-character-weighted densities of states, which might yield insight into why the in-plane polarization gap generally limits the complete gap width. Third, quantitatively correlating the band-edge shifts with the close-pair tail of the nearest-neighbor distribution and the large-pore tail of the pore-size distribution could guide optimization schemes that suppress nearly contacting inclusion pairs and large matrix pores during the generation of ultradense stealthy hyperuniform templates. Such targeted optimization may provide a practical route to disordered phononic composites with even wider, robust, and direction-independent complete elastic-wave gaps.

Finally, a direct experimental test could involve the established millimeter-scale platform of Vasseur et al.: aligned 4 mm-diameter steel cylinders in epoxy with $a = 6.023$ mm, for which ultrasonic band gaps were observed 4). Using the disk positions of the $\chi = 0.30$, $\phi_2 = 0.60$ ultradense design with ~ 5.26 mm-diameter steel cylinders at this scale is predicted to produce an isotropic and complete ultrasonic band gap. Because overlap of the in-plane and out-of-plane polarization gaps depends on preserving ultradense pore channel structure, fabrication errors must not close the minimum neck width $h_{\min} \simeq 0.116a \simeq 0.699$ mm. If ϵ_x and ϵ_R are the maximum center-position and radius errors, respectively, two neighboring cylinders can shrink a neck by at most $2(\epsilon_x + \epsilon_R)$; thus, the neck remains open if $\epsilon_x + \epsilon_R$ 0.350 mm. This submillimeter requirement is likely achievable using conventional precision machining and assembly. Additive manufacturing and lithographic methods 38–40) could enable analogous aligned-cylinder designs at smaller scales, shifting their gaps from ultrasonic toward hypersonic frequencies.

5. Materials and Methods

5.1. Simulation Details for Stealthy Hyperuniform Packings. We obtain disordered ultradense configurations via a modified version of the collective-coordinate optimization procedure (16). We specifically consider the following potential energy (31, 41, 42):

$$\Phi\ \mathbf{r}^N) = \frac{N}{2V} \sum_{\mathbf{k}} \tilde{v}\ \mathbf{k})S\ \mathbf{k}) + \sum_{i\ j} u\ r_{ij}), \qquad [8]$$

in which V is the volume of the periodic simulation cell, $S\ \mathbf{k})$ is the single-configuration structure factor, $\tilde{v}\ \mathbf{k}) = V\ k)\Theta\ K \quad k)$, and

$$u\ r) = u_0\ \ 1 \quad \frac{r}{\sigma}\Big)^2 \Theta\ \sigma \quad r). \qquad [9]$$

The pair potential Eq. **9** penalizes configurations in which particles are closer than σ. By selecting $V\ k) \geq 0$ (e.g., $V\ k) = 1$), we have that $\Phi\ \mathbf{r}^N) \geq 0$. Furthermore, $\Phi\ \mathbf{r}^N) = 0$ only if $S\ 0 \leq |\mathbf{k}| \quad K) = 0$ and the minimum pair distance is σ. Thus, the ground states of the potential Eq. **8** are ultradense stealthy hyperuniform configurations with exclusion region radius K and minimum pair distance σ. Ground states of the potential Eq. **8** are found numerically using the limited-memory Broyden–Fletcher–Goldfarb–Shanno (L-BFGS) optimization algorithm. See ref. 31 for the specific numerical parameters used in this optimization procedure.

5.2. Phononic Band Structure Simulations. Phononic spectra are computed for the 2D transversely isotropic composites described in Section 1 by solving the elastic Bloch eigenvalue problem in a periodic supercell using the finite-element method (5). Because the inclusions are infinitely long and the constituent phases are elastically isotropic, the problem separates into different equations for out-of-plane and in-plane polarized modes, which are treated independently. For general Bloch wavevector $\mathbf{k}$, we solve the corresponding generalized Hermitian eigenvalue problem for the periodic Bloch amplitudes subject to Bloch boundary conditions on the supercell. The finite-element discretization is implemented in MFEM (43) on periodic triangular meshes generated with Gmsh (44), with adaptive refinement in narrow matrix gaps. The resulting generalized Hermitian eigenvalue problems are solved through MFEM s PETSc/SLEPc interface (45, 46) using shift-and-invert spectral transformation and MUMPS sparse factorizations (47, 48).

For each $N = 400$ realization, we compute the lowest $3N$ out-of-plane modes and the lowest $4N$ in-plane modes, which is sufficient to resolve all gaps discussed in the main text. For each χ value considered in the $N = 4{,}000$ calculations, we used the band-edge frequencies extracted from the corresponding $N = 400$ spectra as shift-and-invert targets and computed the lowest 600 eigenfrequencies below and above those edges for each polarization separately. All simulations were repeated with finer meshes and a larger number of requested eigenpairs for representative parameter sets to confirm that the reported gap locations and tail behaviors were numerically converged.

The material parameters of the linearly elastic phases are as follows. The epoxy matrix has mass density $\rho_m^{1)} = 1.1$ g/cm^3, transverse wave speed $c_T^{1)} = 1{,}138$ m/s, and longitudinal wave speed $c_L^{1)} = 2{,}570$ m/s. The steel inclusions have mass density $\rho_m^{2)} = 7.8$ g/cm^3, transverse wave speed $c_T^{2)} = 3{,}286$ m/s, and longitudinal wave speed $c_L^{2)} = 5{,}825$ m/s (4, 5).

5.3. Ensemble Averaging Density of States and Band-Tail Fits. For the $N = 400$ calculations, the density of states and gap statistics are averaged over ensembles of 1,000 independent realizations for each $\chi, \phi_2)$ pair. For the $N = 4{,}000$ calculations, density-of-states and band-tail results are averaged over 2,000 realizations for each χ at $\phi_2 = 0.40$. At the point, the finite-system density of states in Eq. **2** is approximated by binning the computed eigenfrequencies into histograms and normalizing by the supercell area (21). The out-of-plane candidate gap is identified between the Nth and $N + 1)$th eigenfrequencies, and the in-plane candidate gap is identified between the $3N$th and $3N + 1)$th eigenfrequencies. A complete phononic band gap is recorded when the out-of-plane and in-plane polarization gaps overlap in frequency. Gap widths and gap-midgap ratios are computed independently for each realization and then averaged over the ensemble.

To analyze apparent gap persistence at large system size, we compute ensemble-averaged, area-normalized density of states histograms using linear frequency bins,

$$\omega_i) \approx \frac{N_i}{N_{\text{ens}} A\, \Delta\omega_{\text{bin}}}, \qquad [1\ ]$$

where N_i is the number of eigenfrequencies in bin i, N_{ens} is the number of contributing realizations, A is the supercell area, and $\Delta\omega_{\text{bin}}$ is the bin width. For the out-of-plane spectra, we use $\Delta\omega_{\text{bin,OP}} = 0.0025$. Because the in-plane spectra contain approximately three times as many modes over comparable frequency intervals, we use $\Delta\omega_{\text{bin,IP}} = \Delta\omega_{\text{bin,OP}}/3$ for the in-plane histograms and normalize by the corresponding bin width. Power-law tails are fit directly to the binned $\omega)$ in log–log coordinates, $|\delta\omega_\pm|) \sim |\delta\omega_\pm|^{\gamma_\pm}$, while exponential tails are assessed in semilog coordinates.

5.4. Concentration Factor Calculations. The kinetic- and strain-energy concentration factors (22, 23) in each phase i are respectively given by the integrals

$$K^{\ i)} = \frac{\int_{\ i} \rho_m\ \mathbf{x})|\mathbf{u}\ \mathbf{x})|^2 d\mathbf{x}}{\int \rho_m\ \mathbf{x})|\mathbf{u}\ \mathbf{x})|^2 d\mathbf{x}} \qquad [11]$$

Downloaded from https://www.pnas.org by PRINCETON UNIV LIBRARY; ACQUISITION SERVICE PERIODICALS on September 18, 2026 from IP address 140.180.240.88.

and

$$U^{i)} = \frac{\int_{i} \mathbf{x}) : \mathbf{C}\ \mathbf{x}) : \quad \mathbf{x}) d\mathbf{x}}{\int \mathbf{x}) : \mathbf{C}\ \mathbf{x}) : \quad \mathbf{x}) d\mathbf{x}}. \qquad [12]$$

Data Materials and Software Availability. All study data are included in the article and/or *SI Appendix*.

ACKNOWLEDGMENTS. This work was supported by the Army Research Office and was accomplished under Cooperative Agreement No. W911NF-22-2-0103. M.S. thanks Sarah M. Gernhart for helpful discussions, and acknowledges the support of the Harold W. Dodds Honorific Fellowship. We thank the Princeton Institute for Computational Science and Engineering for computational resources.

Author affiliations: [a]Princeton Materials Institute, Princeton University, Princeton, NJ 08544; [b]Department of Physics, Princeton University, Princeton, NJ 08544; [c]Department of Chemistry, Princeton University, Princeton, NJ 08544; and [d]Program in Applied and Computational Mathematics, Princeton University, Princeton, NJ 08544

1. M. Sigalas, E. Economou, Band structure of elastic waves in two dimensional systems. *Solid State Commun* **86**, 141–143 (1993).
2. R. Esquivel-Sirvent, G. H. Cocoletzi, Band structure for the propagation of elastic waves in superlattices. *J Acoust Soc Am* **95**, 86–90 (1994).
3. M. S. Kushwaha, P. Halevi, Band-gap engineering in periodic elastic composites. *Appl Phys Lett* **64**, 1085–1087 (1994).
4. J. O. Vasseur *et al*., Experimental and theoretical evidence for the existence of absolute acoustic band gaps in two-dimensional solid phononic crystals. *Phys Rev Lett* **86**, 3012–3015 (2001).
5. V. Laude, *Phononic Crystals* (De Gruyter, Berlin, Boston, 2020).
6. T. Vasileiadis *et al*., Progress and perspectives on phononic crystals. *J Appl Phys* **129**, 160901 (2021).
7. A. J. O Connor, J. L. Lebowitz, Heat conduction and sound transmission in isotopically disordered harmonic crystals. *J Math Phys* **15**, 692–703 (1974).
8. M. Maldovan, Sound and heat revolutions in phononics. *Nature* **5 3**, 209–217 (2013).
9. N. Zen, T. A. Puurtinen, T. J. Isotalo, S. Chaudhuri, I. J. Maasilta, Engineering thermal conductance using a two-dimensional phononic crystal. *Nat Commun* **5**, 3435 (2014).
10. J. Maire *et al*., Heat conduction tuning by wave nature of phonons. *Sci Adv* **3**, e1700027 (2017).
11. B. L. Davis, M. I. Hussein, Nanophononic metamaterial: Thermal conductivity reduction by local resonance. *Phys Rev Lett* **112**, 055505 (2014).
12. A. Sukhovich, L. Jing, J. H. Page, Negative refraction and focusing of ultrasound in two-dimensional phononic crystals. *Phys Rev B* **77**, 014301 (2008).
13. A. L. Chen, Y. S. Wang, J. B. Li, C. Zhang, Localisation of elastic waves in two-dimensional randomly disordered solid phononic crystals. *Waves Random Complex Media* **2** , 104–121 (2010).
14. O. U. Uche, F. H. Stillinger, S. Torquato, Constraints on collective density variables: Two dimensions. *Phys Rev E* **7** , 046122 (2004).
15. R. D. Batten, F. H. Stillinger, S. Torquato, Classical disordered ground states: Super-ideal gases, and stealth and equi-luminous materials. *J Appl Phys* **1 4**, 033504 (2008).
16. S. Torquato, G. Zhang, F. H. Stillinger, Ensemble theory for stealthy hyperuniform disordered ground states. *Phys Rev X* **5**, 021020 (2015).
17. S. Torquato, Hyperuniform states of matter. *Phys Rep* **745**, 1–95 (2018).
18. M. Florescu, S. Torquato, P. J. Steinhardt, Designer disordered materials with large complete photonic band gaps. *Proc Nat Acad Sci U S A* **1 6**, 20658–20663 (2009).
19. W. Man *et al*., Photonic band gap in isotropic hyperuniform disordered solids with low dielectric contrast. *Opt Express* **21**, 19972–19981 (2013).
20. W. Man *et al*., Isotropic band gaps and freeform waveguides observed in hyperuniform disordered photonic solids. *Proc Nat Acad Sci U S A* **11** , 15886–15891 (2013).
21. M. Klatt, P. Steinhardt, S. Torquato, Wave propagation and band tails of two-dimensional disordered systems in the thermodynamic limit. *Proc Natl Acad Sci U S A* **119**, e2213633119 (2022).
22. J. D. Joannopoulos, S. G. Johnson, J. N. Winn, R. D. Meade, *Photonic Crystals: Molding the Flow of Light* (Princeton University Press, Princeton, New Jersey, ed. 2, 2008).
23. G. Gkantzounis, T. Amoah, M. Florescu, Hyperuniform disordered phononic structures. *Phys Rev B* **95**, 094120 (2017).
24. A. Rohfritsch, J. M. Conoir, T. Valier-Brasier, R. Marchiano, Impact of particle size and multiple scattering on the propagation of waves in stealthy-hyperuniform media. *Phys Rev E* **1 2**, 053001 (2020).
25. V. Romero-García *et al*., Wave transport in 1d stealthy hyperuniform phononic materials made of non-resonant and resonant scatterers. *APL Mater* **9**, 101101 (2021).
26. T. Valier-Brasier, A. Rohfritsch, J. M. Conoir, R. Marchiano, Propagation of coherent longitudinal and shear waves in two-dimensional elastic media with randomly distributed resonant cavities. *Phys Rev B* **1 5**, 054310 (2022).
27. L. Alhaïtz, J. M. Conoir, T. Valier-Brasier, Experimental evidence of isotropic transparency and complete band gap formation for ultrasound propagation in stealthy hyperuniform media. *Phys Rev E* **1 8**, 065001 (2023).
28. M. Diego *et al*., Hypersonic acoustic wave control via stealthy hyperuniform phononic nanostructures. *Sci Adv* **11**, eadw7205 (2025).
29. T. Valier-Brasier, Propagation of coherent mechanical waves in stealth hyperuniform materials in the transparent regime. *Phys Rev E* **113**, 065505 (2026).
30. S. Torquato, J. Kim, Existence of nonequilibrium glasses in the degenerate stealthy hyperuniform ground-state manifold. *Soft Matter* **21**, 4898–4907 (2025).
31. J. Kim, S. Torquato, Ultradense sphere packings derived from disordered stealthy hyperuniform ground states. *J Chem Phys* **163**, 024902 (2025).
32. G. Zhang, F. H. Stillinger, S. Torquato, Transport, geometrical and topological properties of stealthy disordered hyperuniform two-phase systems. *J Chem Phys* **145**, 244109 (2016).
33. G. Zhang, F. H. Stillinger, S. Torquato, Can exotic disordered "stealthy" particle configurations tolerate arbitrarily large holes? *Soft Matter* **13**, 6197–6207 (2017).
34. C. Vanoni, J. Kim, P. J. Steinhardt, S. Torquato, Dynamical properties of particulate composites derived from ultradense stealthy hyperuniform sphere packings. *Phys Rev E* **112**, 015406 (2025).
35. G. Zhang, F. Stillinger, S. Torquato, Ground states of stealthy hyperuniform potentials: II. Stacked-slider phases. *Phys Rev E* **92**, 022120 (2015).
36. S. Torquato, *Random Heterogeneous Materials: Microstructure and Macroscopic Properties* (Springer-Verlag, New York, 2002).
37. A. Chen, S. Torquato, "Geometrical and topological properties of disordered ultradense stealthy hyperuniform disk packings" in *Preparation*, (2026).
38. K. Zhao, T. G. Mason, Assembly of colloidal particles in solution. *Rep Prog Phys* **81**, 126601 (2018).
39. M. Vaezi, H. Seitz, S. Yang, A review on 3d micro-additive manufacturing technologies. *Int J Adv Manuf Technol* **67**, 1721–1754 (2013).
40. S. F. S. Shirazi *et al*., A review on powder-based additive manufacturing for tissue engineering: Selective laser sintering and inkjet 3d printing. *Sci Tech Adv Mater* **16**, 033502 (2015).
41. J. Kim, S. Torquato, Multifunctional composites for elastic and electromagnetic wave propagation. *Proc Nat Acad Sci U S A* **117**, 8764–8774 (2020).
42. S. Torquato, J. Kim, Nonlocal effective electromagnetic wave characteristics of composite media: Beyond the quasistatic regime. *Phys Rev X* **11**, 021002 (2021).
43. R. Anderson *et al*., MFEM: A modular finite element methods library. *Comput Math Appl* **81**, 42–74 (2021).
44. C. Geuzaine, J. F. Remacle, Gmsh: A 3-d finite element mesh generator with built-in pre- and post-processing facilities. *Int J Numer Methods Eng* **79**, 1309–1331 (2009).
45. S. Balay, W. D. Gropp, L. C. McInnes, B. F. Smith, "Efficient management of parallelism in object oriented numerical software libraries" in *Modern Software Tools in Scientific Computing*, E. Arge, A. M. Bruaset, H. P. Langtangen, Eds. (Birkhäuser Press, 1997), pp. 163–202.
46. V. Hernandez, J. E. Roman, V. Vidal, SLEPc: A scalable and flexible toolkit for the solution of eigenvalue problems. *ACM Trans Math Softw* **31**, 351–362 (2005).
47. P. Amestoy, I. S. Duff, J. Koster, J. Y. L Excellent, A fully asynchronous multifrontal solver using distributed dynamic scheduling. *SIAM J Matrix Analysis Appl* **23**, 15–41 (2001).
48. P. Amestoy, A. Buttari, J. Y. L Excellent, T. Mary, Performance and scalability of the block low-rank multifrontal factorization on multicore architectures. *ACM Trans Math Softw* **45**, 2:1–2:26 (2019).

Downloaded from https://www.pnas.org by PRINCETON UNIV LIBRARY; ACQUISITION SERVICE PERIODICALS on September 18, 2026 from IP address 140.180.240.88.